

Optical phonons in the $\text{NaTiSi}_2\text{O}_6$ oxide with $S = \frac{1}{2}$ spin chains

Z. V. Popović,^{1,2} M. J. Konstantinović,¹ V. N. Popov,³ A. Cantarero,² Z. Dohčević-Mitrović,¹ M. Isobe,⁴ and Y. Ueda⁴

¹Center for Solid State Physics and New Materials, Institute of Physics, P.O. Box 68, 11080 Belgrade, Serbia

²Materials Science Institute, University of Valencia, P.O. Box 22085, 46071 Valencia, Spain

³Faculty of Physics, University of Sofia, 1126 Sofia, Bulgaria

⁴Materials Design and Characterization Laboratory, Institute for Solid State Physics, The University of Tokyo, 5-1-5 Kashiwanoha,

Kashiwa, Chiba 277-8581, Japan

(Received 14 April 2004; published 15 June 2005)

We have measured infrared reflectivity and Raman scattering spectra of $\text{NaTiSi}_2\text{O}_6$ at different temperatures. We have observed almost all infrared and Raman active modes predicted by factor-group analysis for monoclinic symmetry of $\text{NaTiSi}_2\text{O}_6$. The infrared-active phonon frequencies are obtained by Kramers-Kronig analysis of the reflectivity data. The assignment of the observed modes is done using lattice dynamical calculations based on the valence shell model. A phase transition at about 210 K is manifested through a dramatic change of the mode frequency and broadening, and the appearance of new phonon modes. Analyzing the phonon frequency and damping vs temperature we have found that the phase transition leaves a fingerprint in the phonon dynamics of $\text{NaTiSi}_2\text{O}_6$.

DOI: 10.1103/PhysRevB.71.224302

PACS number(s): 78.30.Hv, 63.20.Dj, 64.70.Kb, 75.10.-b

I. INTRODUCTION

Minerals of the pyroxene group ($AMB_2\text{O}_6$, A =alkali metal; B =Si, Ge; M =trivalent ions of $3d$ transition metals) are one of the most abundant rock-forming minerals on Earth. They have received increasing attention from both mineralogists and petrologists in the last several decades.¹ Recently, the pyroxene compounds with transition metal ions $M^{3+}=\text{Ti}$, V ,²⁻¹² have drawn great attention as low-dimensional magnets. Among them, $\text{NaTiSi}_2\text{O}_6$ is of particular interest²⁻⁶ because it is an $S = \frac{1}{2}$ chain system, that differs from other $S \neq \frac{1}{2}$ pyroxenes⁷⁻¹² due to the lack of low-temperature antiferromagnetic order, and instead shows signs of opening a spin gap.²

The structure of pyroxenes can be described in terms of alternating tetrahedral and octahedral layers that lie parallel to the (100) plane, Fig. 1(a). Within the tetrahedral layer each tetrahedron shares two corners with adjacent tetrahedra to form infinite chains parallel to the c axis, Fig. 1(b). The base of each tetrahedron lies approximately in the (100) plane and the repeat unit in each chain consists of two tetrahedra with the formula $(\text{SiO}_3)^{2-}$. The octahedral layer contains isolated chains of edge-sharing TiO_6 octahedra. Because of edge-sharing the octahedral chain looks like a zigzag chain formed by Ti_2O_{10} dimers.

The magnetic moments in pyroxenes come from the M ions, with different spins depending on the ionic states (Ti^{3+} corresponds to $S = \frac{1}{2}$, V^{3+} to $S = 1$, and Cr^{3+} to $S = \frac{3}{2}$). At room temperature, all Ti ions are at the same crystallographic site,^{3,13} and the chains can be regarded as uniform linear chains with $S = \frac{1}{2}$. The magnetic susceptibility measurements of $\text{NaTiSi}_2\text{O}_6$ show Curie-Weiss behavior at high temperatures, followed by sharp decrease below the critical temperature $T_c = 210$ K, which is argued to be the indication of opening a spin-gap.² Below T_c a dimerization of Ti—Ti distances along the chain was observed by the x-ray scattering.³ The phase transition in $\text{NaTiSi}_2\text{O}_6$ is described as an orbital

order-disorder type of the phase transition with concomitant magnetic and lattice changes. Moreover, Konstantinović *et al.*⁴ shown that the t_{2g} orbitals of Ti^{3+} ions dominate the exchange and fluctuations and argued that the phase transition in $\text{NaTiSi}_2\text{O}_6$ can be regarded as an orbital analogue of the spin-Peierls phase transition.

The previous Raman scattering study⁵ has revealed the existence of phonon anomalies at T_c and a large phonon broadening in the room temperature spectra of $\text{NaTiSi}_2\text{O}_6$. The microscopic orbital-spin model⁵ shows that the difference between $S = \frac{1}{2}$ and $S \neq \frac{1}{2}$ pyroxenes originates from a unique interplay between electronic anisotropy (quasi-one-dimensional), and t_{2g} orbital degeneracy, and suggests that the quasi-one-dimensional dynamical Jahn-Teller phase of $\text{NaTiSi}_2\text{O}_6$ exhibits a spontaneous breaking of the translational symmetry into a dimerized orbital ordered state with a spin gap due to the formation of spin valence bonds.

Using a density functional approach, Popović *et al.*⁶ calculated the electronic structure of $\text{NaTiSi}_2\text{O}_6$ and found that the structure with mixed antiferromagnetic-ferromagnetic order is favorable in the ground state at low temperatures. Their model includes the ferromagnetic ordering of spins inside Ti—Ti crystallographic dimers in the low temperature phase of $\text{NaTiSi}_2\text{O}_6$, and antiferromagnetic ordering between them.

Many of the physical properties of $\text{NaTiSi}_2\text{O}_6$, including lattice dynamics, are unknown. Here we report the reflectivity spectra and Raman scattering of $\text{NaTiSi}_2\text{O}_6$ samples at different temperatures. We observed 29 Raman and 22 infrared active modes (one Raman and five infrared modes less than predicted by factor-group analysis for monoclinic symmetry of $\text{NaTiSi}_2\text{O}_6$). The assignment of the observed modes is done using lattice dynamical calculations based on the shell valence model. The phase transition at about 210 K is manifested through a steep change of the mode frequency, its broadening and the appearance of new phonon modes. The temperature dependence of phonon frequency and damping

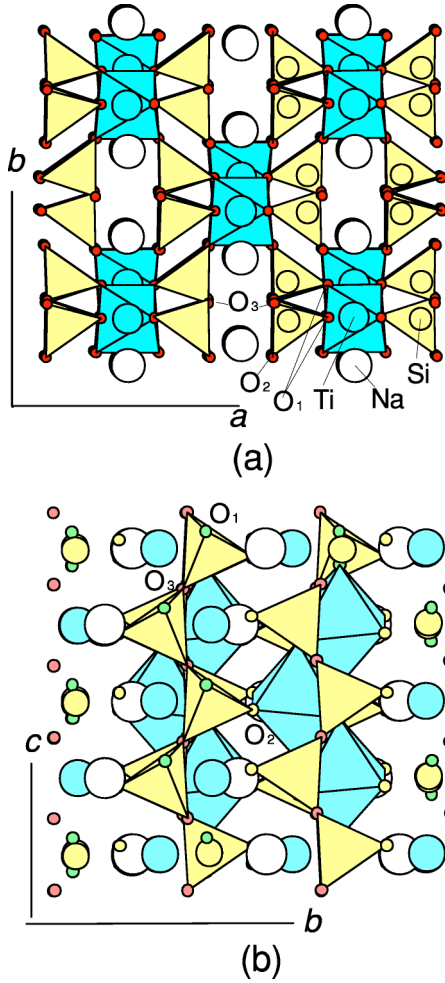


FIG. 1. A schematic illustration of the $\text{NaTiSi}_2\text{O}_6$ pyroxene structure in (a) the (001) plane and (b) the (100) plane.

shows that the phase transition has a strong influence on the phonon dynamics of $\text{NaTiSi}_2\text{O}_6$.

II. EXPERIMENT

Powder samples of $\text{NaTiSi}_2\text{O}_6$ were prepared by a solid-state reaction of mixtures with an appropriate molar ratio of $\text{Na}_2\text{TiSi}_4\text{O}_{11}$, Ti, and TiO_2 . The weighted mixtures were pressed into pellets and heated at 1050°C in an evacuated silica tube for several days. X-ray diffraction measurements show a single phase behavior.²

Reflectivity spectra were measured from polished polycrystalline pellets with a BOMEM DA-8 spectrometer. A DTGS pyroelectric detector was used to cover the frequency region from 80 to 600 cm^{-1} ; a liquid-nitrogen cooled Hg—Cd—Te detector was used from 500 to 6000 cm^{-1} . Spectra were collected with 2 cm^{-1} resolution, with 1000 interferograms added for each spectrum. For low-temperature measurements (80 – 300 K) a Janis STDA 100 cryostat was used. The far-infrared reflectivity spectra at liquid helium temperature were measured using a Bruker 113v spectrometer with a Oxford cryostat and a Si-bolometer as detector.

The Raman spectra were measured using a micro-Raman system coupled to a DILOR triple spectrometer including a liquid nitrogen cooled charge-coupled-device detector. The 514.5 nm line of an Ar-ion laser was used as excitation source. Low-temperature measurements were carried out in an Oxford continuous flow cryostat with a 0.5 mm thick window. The laser beam was focused by a long working distance ($\sim 10\text{ mm}$ focal length) microscope objective (magnification $50\times$). In order to guarantee that the Raman spectra are not influenced by resonances or temperature effects (sample overheating), we performed the measurements using different laser lines and intensities, obtaining almost identical spectra.

III. RESULTS AND ANALYSIS

A. Factor-group analysis

Sodium titanium metasilicate, $\text{NaTiSi}_2\text{O}_6$, crystallizes in a monoclinic unit cell with a space group $C2/c$. The room temperature unit cell parameters are $a=0.9692\text{ nm}$, $b=0.8874\text{ nm}$, $c=0.5301\text{ nm}$, and $\beta=106.85^\circ$.¹³ The unit cell of $\text{NaTiSi}_2\text{O}_6$ consists of four formula units ($Z=4$) with 40 atoms in all (20 atoms per primitive cell). The site symmetry of Na, Ti, Si, O_1 , O_2 , and O_3 atoms in the $C2/c$ (C_{2h}^6) space group are (4e), (4e), (8f), (8f), (8f), and (8f), respectively. The factor-group-analysis (FGA) yields

$$(\text{Na,Ti})(C_2):\Gamma = A_g + A_u + 2B_{1g} + 2B_u,$$

$$(\text{Si,O}_1,\text{O}_2,\text{O}_3)(C_1):\Gamma = 3A_g + 3A_u + 3B_g + 3B_u.$$

Summarizing these representations and subtracting the acoustic ($A_u + 2B_u$) modes, we obtained the following irreducible representations of $\text{NaTiSi}_2\text{O}_6$ vibrational modes in the $C2/c$ space group:

$$\begin{aligned} \Gamma_{\text{NaTiSi}_2\text{O}_6}^{\text{opt}}(C2/c) = & 14A_g(xx,yy,zz,xz) + 16B_g(xy,yz) \\ & + 13A_u(\mathbf{E}\parallel y) + 14B_u(\mathbf{E}\parallel x,\mathbf{E}\parallel z). \end{aligned}$$

Thus, 27 infrared and 30 Raman active modes are expected to be observed in the $\text{NaTiSi}_2\text{O}_6$ spectra at room temperature (above the phase transition temperature).

$\text{NaTiSi}_2\text{O}_6$ undergoes a phase transition at $T_c \approx 210\text{ K}$. The low temperature phase has been identified as triclinic,³ space group $P\bar{1}$, with two formula units per unit cell ($Z=2$). All atoms have C_i position symmetry of $P\bar{1}$ space group. Consequently, the irreducible representation of $\text{NaTiSi}_2\text{O}_6$ vibrational modes of $P\bar{1}$ space group is

$$\Gamma_{\text{NaTiSi}_2\text{O}_6}^{\text{opt}}(P\bar{1}) = 30A_g + 27A_u,$$

since $3A_u$ are acoustic modes.

B. Lattice dynamics

A valence shell model (VSM) is used for the calculation of the lattice dynamics of $\text{NaTiSi}_2\text{O}_6$. The VSM is a combination of the shell model with the valence-force-field (VFF) model proposed by Kunc and Bilz¹⁴ for the case of

TABLE I. Lattice dynamics parameters (V is the unit cell volume).

Atoms	Na	Ti	Si	O
Ionic charge Z (in $ e $)	0.95	0.73	1.61	-0.82
Shell charge Y (in $ e $)	3.05	2.66	0.85	-3.31
Polarizability α (\AA^3)	0.44	0.31	0.31	0.94
VFF parameters (in units e^2/V)	Bond stretching		Bond bending	
	Ti-O	778	Ti-O-Ti	40
	Si-O	996	O-Ti-O	27
			Si-O-Si	132
			O-Si-O	-10
			Si-O-Ti	18
BM potential parameters			A (in eV)	B (in \AA^{-1})
	Na-O		753	1.75

zincblende compounds. In this model, the long-range interactions are described by Coulomb potentials. The short-range interactions are described by valence force field parameters of the types nearest-neighbor bond-stretching parameters for the bonds Ti-O and Si-O, and bond-bending parameters for the bond angles Ti-O-Ti, O-Ti-O, Si-O-Si, O-Si-O, and Si-O-Ti. The short-range interactions between Na and O are modeled by a Born-Mayer (BM) potential Ae^{-Br} , where r is the interatomic separation and A and B are parameters. Each atom is ascribed an ionic charge Z and is represented as a point charged core with spherical massless shell around it with a shell charge Y . The shell is coupled to the core by a force constant k and the ionic polarizability α is given by Y^2/k . The total number of model parameters is $3Z+4Y+4\alpha+7\text{VFF}+2\text{BM}=20$. The number of parameters has been kept as low as possible. The parameters are determined by use of the equilibrium condition and fitting to the highest frequency Raman-active (A_g and B_g) modes. In the case of Si and O ions and Si-O interactions the input parameters are taken from alpha-quartz. The model parameters are given in Table I.

There is an overall good agreement of the experimental data with the largest deviations not exceeding 10%. The modes in the spectral range between 150 and 600 cm^{-1} are bond-bending vibrations, while the higher frequency modes originate from bond-stretching vibrations. The full assignment of all optical modes is given in Tables II and III and we do not repeat it here for conciseness.

C. Results

Figure 2 shows the reflectivity spectra of NaTi(V)Si₂O₆ measured at room and liquid nitrogen temperatures in the spectral range between 100 and 1200 cm^{-1} . The low temperature reflectivity spectrum differs from the room temperature one, due to the NaTiSi₂O₆ crystal structure and symmetry change below the phase transition temperature ($T_c=210$ K).³ The TO and LO mode frequencies of infrared phonons, collected in Table II, are obtained using a Kramers-Kronig analysis to the reflectivity data. Graphic illustration

of TO and LO frequency changes by lowering the temperature for three oscillators in the 210–255 cm^{-1} spectral range are given in Fig. 3. As can be seen from Fig. 3, the TO and LO frequencies change smoothly between a room temperature and the phase transition temperature. By further temperature decrease a dramatic frequency change is found for almost all mode frequencies. In addition, new modes appear in the reflectivity spectra of NaTiSi₂O₆. In Fig. 4 we show the infrared spectra of NaTiSi₂O₆ in the 350–410 cm^{-1} range. Appearance of new modes below 200 K coincides with the phase transition temperature.

The unpolarized room temperature Raman spectra of NaTiSi₂O₆ in the spectral range between 100 and 1100 cm^{-1} are given in Fig. 5(a). The low temperature (10 K) Raman spectra of the same sample are given in Fig. 5(b). The frequencies of all observed Raman modes of NaTiSi₂O₆ are collected in Table III. By lowering the temperature, the Raman modes of NaTiSi₂O₆ become narrower and they dramatically change their energy and broadening, at the phase transition temperature, as it is illustrated in Figs. 5 and 6 and discussed in the Sect. IV.

IV. DISCUSSION

As we mentioned above, the low temperature phase of NaTiSi₂O₆ has triclinic crystal structure and $P\bar{1}$ space group. The compatibility diagram (see the inset of Fig. 4) between $C2/c$ and $P\bar{1}$ space groups indicates that the B_g (B_u) symmetry modes become of A_g (A_u) symmetry in the low temperature phase. Thus, low temperature Raman (infrared) spectrum consists only of A_g (A_u) symmetry modes. The total number of infrared and Raman active modes in both high and low temperature phase remains unchanged.

Because of the lack of single crystals, our infrared and Raman spectra were measured with unpolarized light. Consequently, room temperature infrared (Raman) spectra, Fig. 2 (Fig. 5), contain the modes of both the A_u (A_g) and B_u (B_g) symmetry. We clearly observe 20 infrared (Table II) and 21 Raman (Table III) active modes at room temperature. The

TABLE II. Infrared active mode frequencies (in cm^{-1}) of $\text{NaTiSi}_2\text{O}_6$.

ν_i	Sym.	Experiment				Calculation		Assignment
		300 K		10 K		TO	LO	
		TO	LO	TO	LO	TO	LO	
1	B_u^1	119.1	126.8	121.5	128.3	138	142	$\text{Na}\parallel z$
2	A_u^1	143.7	152.3	150.4	153.8	156	173	$\text{O}_3+\text{Na}\parallel y$
3	B_u^2	189.5	197.7	192.4	199.1	198	201	$\text{O}_3+\text{Na}\parallel xz$
4	B_u^3	209.7	224.7	213.1	221.8	206	245	$\text{O}_1\text{-Si-O}_2$ bending
5	A_u^2			230.9	235.8	233	250	$\text{O}_1\text{-Si-O}_2$ bending
6	B_u^4	238.2	248.3	250.7	254.6	249	292	$\text{O}_2+\text{Na}\parallel xz$
7	A_u^3	255.0	265.6	258.9	275.8	283	285	$\text{O}_1\text{-Si-O}_2$ bending+ $\text{Na}\parallel y$
8	A_u^4	278.7	285.9	281.1	293.6	301	302	$\text{O}_2\text{-Si-O}_3$ bending+ $\text{Na}\parallel y$
9	B_u^5	292.2	321.1	297.5	327.8	327	333	$\text{O}_1\text{-Si-O}_2$ bending+ $\text{Na}\parallel xz$
10	B_u^6	356.8	377.5	362.6	366.4	349	351	$\text{O}_1\text{-Si-O}_2$ bending+ $\text{Na}\parallel xz$
11	B_u^7	387.1	393.9	386.2	391.0	376	382	$\text{O}_2\text{-Si-O}_3$ bending
12	A_u^5	411.2	426.2	433.4	466.2	392	402	$(\text{O}_1\text{-Ti-O}_2), (\text{O}_1\text{-Si-O}_2)$ bending
13	A_u^6	463.8	511.0	466.2	513.0	468	471	$\text{Si-O}_{1,2}$ stretching
14	A_u^7					509	539	$\text{Si-O}_{1,2}$ stretching
15	B_u^8	546.2	585.3	545.8	582.9	531	564	$\text{Ti-O}_{1,2}, \text{Si-O}_{1,2}$ stretching
16	B_u^9					593	596	$\text{Ti-O}_2, \text{Si-O}_{1,2}$ stretching
17	A_u^8	636.4	652.8	641.2	652.8	615	615	$\text{Ti-O}_{1,2}, \text{Si-O}_{1,2}$ stretching
18	B_u^{10}					696	699	Si-O_3 stretching
19	A_u^9	719.3	729.9	726.1	730.9	748	748	$\text{O}_3\parallel x$
20	B_u^{11}					823	823	Si-O_3 stretching
21	A_u^{10}	864.0	877.5	875.5	883.3	865	867	$\text{Si-O}_{1,3}$ stretching
22	A_u^{11}	895.8	931.5	897.7	944.0	910	911	$\text{Si-O}_{1,2}$ stretching
23	B_u^{12}	948.8	961.3	950.7	959.4	959	965	Ti-O_2 stretching
24	A_u^{12}	999.9	1024.9	983.5	1005.7	979	990	$\text{Ti-O}_{1,2}$ stretching
25	B_u^{13}					987	994	Ti-O_1 stretching
26	B_u^{14}			1022.1	1028.8	1020	1029	Ti-O_1 stretching
27	A_u^{13}	1039.7	1089.5	1037.5	1095.3	1037	1037	$\text{TiO}_6, \text{SiO}_4$ breathing

missing modes (seven infrared and nine Raman) are either of very low intensity or masked by modes of other symmetry. Below the phase transition temperature two additional infrared and eight Raman modes appear.

By lowering the temperature, dramatic changes (appearance of new modes or mode splitting) appear in our Raman and infrared spectra at the positions where modes of the different symmetry have nearly the same energy. At the phase transition temperature, the antisymmetric (B) modes become symmetric (A), and the modes closed in energy start to couple. As a consequence, a mode repulsion appears. An illustration of such effect is given in the inset of Fig. 5(a) for the $208/221 \text{ cm}^{-1}$ Raman mode pair. Frequency and intensity exchange of these modes is known as the anticrossing effect (mixing of modes with equal symmetry).

In the inset of Fig. 5(b) we show the temperature dependence of the frequency (ω) and broadening Γ [full width at half-maximum (FWHM)] of 388 cm^{-1} mode, obtained by the Lorentzian profile fitting procedure. This mode is isolated, that means it does not couple with surrounding Raman

modes in the low temperature phase. The frequency of the mode increases monotonously from a room temperature to the phase transition temperature, where a drastic change of frequency is observed. The drastic frequency variation is a consequence of the change of crystal and magnetic structure at the phase transition due to the orbital ordering.⁵ In order to distinguish the phonon-phonon contribution due to anharmonic effects from orbital ordering-related contribution we have fitted the high temperature part (200–300 K) of frequency versus temperature dependence using a model for the anharmonic phonon-phonon scattering,¹⁵

$$\omega_{ph}(T) = \omega_0 + C[1 + 2/(e^x - 1)],$$

where ω_0 and C have the values 395.6 cm^{-1} and -3.2 cm^{-1} , respectively, and $x = \hbar\omega_0/2kT$. The calculated spectra is represented by a dashed line in the inset of Fig. 5(b). It is obvious that the dominant contribution in the frequency versus temperature dependence of the 388 cm^{-1} mode below the phase transition arises from lattice and orbital rearrangement

TABLE III. Raman mode frequencies (in cm⁻¹) of NaTiSi₂O₆.

ν_i	Sym.	Experiment		Calculation	Assignment
		300 K	10 K		
1	B_{1g}^1		108.0	111	(O ₃ -Si-O ₃) bending $\parallel y$
2	A_{1g}^1	150.8	148.4	147	(O ₃ -Si-O ₃) bending $\parallel z$
3	B_{2g}^1	176.6	181.0	165	Na $\parallel z$
4	B_{3g}^1	188.8	189.6	184	(O ₂ -Ti-O ₂), (O ₃ -Si-O ₃) bending+Na $\parallel x$
5	A_{2g}^1	208.6	209.4	195	(O ₃ -Si-O ₃) bending
6	A_{2g}^2	220.8	220.6	212	(O ₂ -Ti-O ₂), (O ₂ -Si-O ₃) bending+Na $\parallel y$
7	B_{2g}^2	266.5	266.8	250	(O ₂ -Ti-O ₂) bending+Na $\parallel z$
8	B_{3g}^2	275.4	275.7	272	(O ₁ -Si-O ₂) bending+Na $\parallel x$
9	A_{4g}^1	304.4	307.3	282	O ₂ $\parallel xz$ +Na $\parallel y$
10	B_{6g}^1		311.8	307	(O ₂ -Si-O ₃) bending+Ti $\parallel x$
11	A_{5g}^1	329.3	326.9	309	(O ₂ -Ti-O ₂) bending
12	B_{7g}^1		348.1	352	O ₂ $\parallel z$
13	A_{6g}^1	388.0	394.8	362	(O ₁ -Ti-O ₁) bending
14	B_{8g}^1		439.6	452	(O ₁ -Ti-O ₁) bending
15	A_{7g}^1	468.2	473.1	466	(O ₁ -Ti-O ₁) bending
16	B_{9g}^1	494.3	499.6	487	(O ₁ -Si-O ₂) bending
17	A_{8g}^1		522.6	537	(O ₁ -Ti-O ₁) bending
18	B_{10g}^1	553.6	549.0	543	(O ₁ -Ti-O ₂), (O ₁ -Si-O ₂) bending
19	A_{9g}^1		573.6	574	TiO ₆ "scissors" bending
20	B_{11g}^1	624.2	626.5	627	(Ti-O ₂), (Si-O ₁) stretching
21	A_{10g}^1	673.3	675.6	693	Si-O ₃ stretching $\parallel x$
22	B_{12g}^1	750.0	753.0	748	Si-O ₃ stretching $\parallel x$
23	A_{11g}^1	837.6	845.7	821	Si-O ₃ stretching $\parallel yz$
24	B_{13g}^1		856.2	870	Si-O ₃ stretching $\parallel yz$
25	A_{12g}^1			908	(Ti-O _{1,2}), (Si-O _{1,2}) stretching
26	B_{14g}^1	947.6	937.9	950	(Ti-O _{1,2}), (Si-O _{1,2}) stretching
27	A_{13g}^1		972.9	958	(Ti-O _{1,2}), (Si-O _{1,2}) stretching
28	B_{15g}^1	963.7	988.1	968	(Ti-O _{1,2}), (Si-O _{1,2}) stretching
29	A_{14g}^1	1023.6	1032.6	1017	TiO ₆ , SiO ₄ breathing
30	B_{16g}^1	1038	1044.0	1047	TiO ₆ (out-of-phase), SiO ₄ breathing

but not from phonon-phonon scattering due to anharmonic effects.

Next, we analyze the frequency versus temperature dependence of the 553 cm⁻¹ mode, Fig. 6(a). This mode first

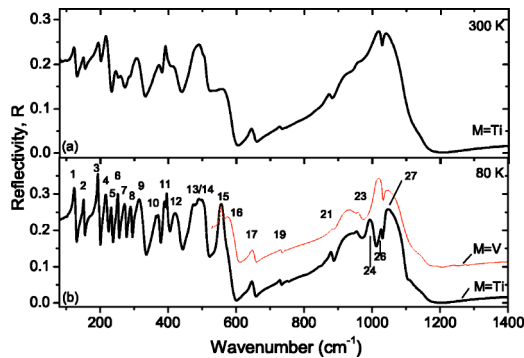


FIG. 2. (a) Room and (b) liquid nitrogen temperature infrared reflectivity spectra of NaTi(V)Si₂O₆.

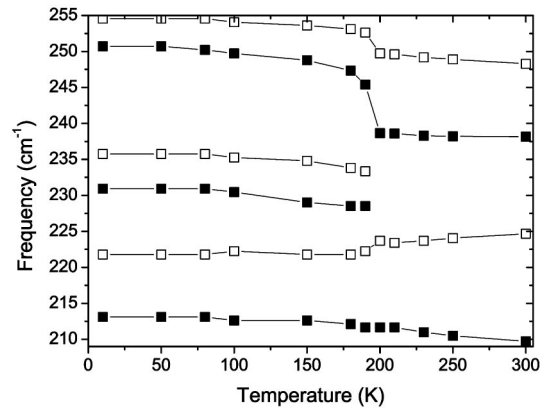


FIG. 3. Temperature dependence of TO (full symbol) and LO (empty symbol) infrared active mode frequencies obtained by Kramers-Kronig analysis of the reflectivity data.

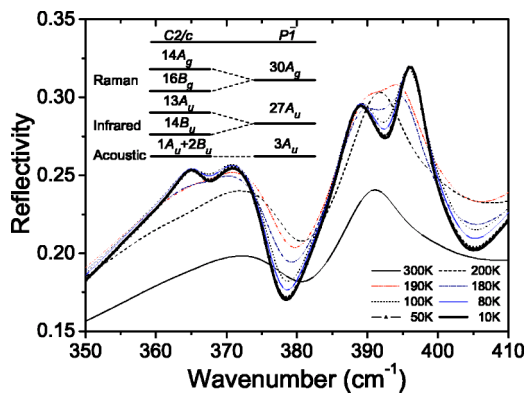


FIG. 4. Far-infrared reflectivity spectra of NaTiSi₂O₆ at different temperatures in the 350 cm⁻¹–410 cm⁻¹ spectral range. Inset, compatibility diagram relating the vibrations of modes of NaTiSi₂O₆ in C2/c and P1 space group.

hardens by temperature lowering and, at about 200 K, starts to soften due to the coupling with a neighboring mode. By further temperature decrease the coupling becomes stronger resulting in a mode repulsion and intensity exchange, see inset of Fig. 6(a).

In Fig. 5(a) we show room temperature Raman spectra of NaTiSi₂O₆ together with the room temperature Raman spectra of NaVSi₂O₆. At a first glance we noted that the phonon lines dramatically broaden in the Ti-pyroxene—an oxide with the smallest spin value. Because of the phonon broadening, the NaTiSi₂O₆ Raman spectrum at 300 K contains effectively less phonon modes than expected by FGA, and observed in V-pyroxene. This effect was discussed in Ref. 5. We concluded there that the fluctuations of the orbital degrees of freedom at high temperatures lead to a dynamic Jahn-Teller phase with anomalous phonon broadening and remnant antiferromagnetic spin fluctuations. These results, combined with the microscopic orbital-spin model that we derive in Ref. 5, suggest that the quasi-one-dimensional dynamical Jahn-Teller phase of NaTiSi₂O₆ exhibits a spontaneous breaking of translational symmetry into a dimerized or-

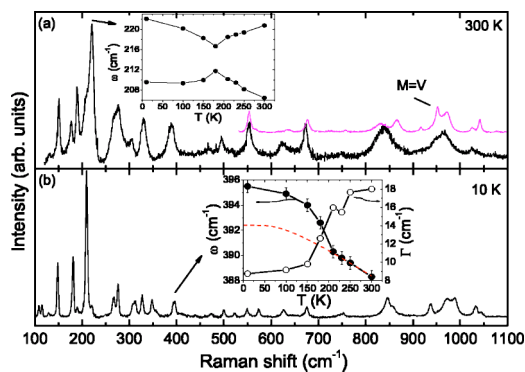


FIG. 5. Raman spectra of the NaTi(V)Si₂O₆ sample measured at room temperature (a) and at 10 K (b). Inset (a), frequency vs temperature dependence of 208/221 cm⁻¹ mode pair. Inset (b), temperature dependence of energy and broadening of 388 cm⁻¹ mode. The dashed line represents the anharmonic phonon-phonon scattering spectrum. The laser excitation wavelength was 514.5 nm.

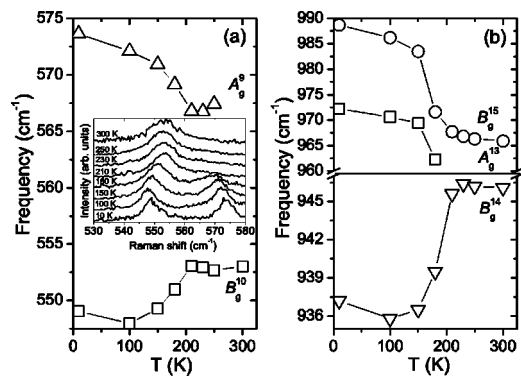


FIG. 6. (a) Temperature dependence of frequency and broadening of the 553 cm⁻¹ Raman mode. Inset, Raman spectra of NaTiSi₂O₆ in the spectral range between 530 cm⁻¹ and 580 cm⁻¹ at different temperatures. (b) Frequency versus temperature dependence for the B_g¹⁴, A_g¹³, and B_g¹⁵ modes.

bital ordered state with a spin gap due to the formation of spin valence bonds.

Frequency and linewidth versus temperature dependence of the broad structure at about 970 cm⁻¹ are given in Fig. 6(b). The mode at about 946 cm⁻¹ softens for about 10 cm⁻¹, while mode at 966 splits, and hardens by 25 cm⁻¹. The FWHM of the 965 cm⁻¹ phonon increases up to the maximum value at about 210 K, and then decreases to the saturation value, see Fig. 7. This means that the bond fluctuations are considerably larger in the high temperature than in the low temperature phase (the proximity of the structural phase transition induces the largest fluctuations, producing the maximum FWHM at T_c).

Figure 7 shows the normalized frequency and broadening for several Raman active modes together with normalized magnetic susceptibility from Ref. 2. We found that the phonon frequency and broadening map well the normalized magnetic susceptibility curve, indicating that the phase transition leaves a fingerprint in the phonon dynamics of NaTiSi₂O₆.

The splitting of infrared oscillators shown in Fig. 4 comes from the appearance of two modes of other symmetry with frequencies close to the room temperature oscillators frequency. The same effect is registered for the highest fre-

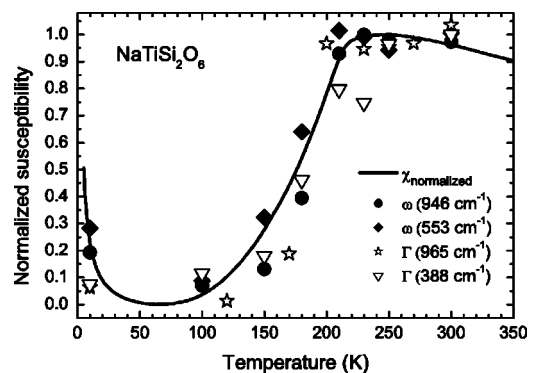


FIG. 7. Temperature dependence of the normalized frequency and damping of several Raman active modes together with the normalized magnetic susceptibility (solid line) of NaTiSi₂O₆, Ref. 2.

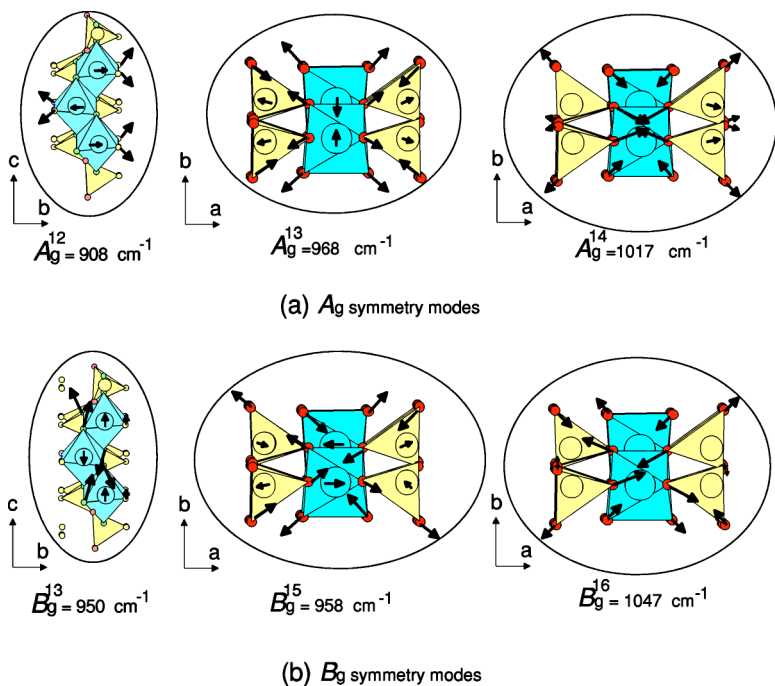


FIG. 8. Ion displacement patterns of high frequency modes of (a) A_g and (b) B_g symmetry in NaTiSi₂O₆.

quency B_u symmetry mode, Fig. 2(b). This mode is completely masked at room temperature by two highest frequency A_u symmetry modes. By lowering the temperature, the B_u mode becomes A_u and the strong coupling between these oscillators leads to the mode repulsion, see Fig. 2(b). Note that such an effect is not observed in the low temperature infrared spectra of isostructural V-pyroxene [Fig. 2(b)].

Finally, in Fig. 8 we show the ionic displacement patterns obtained by the shell model calculation (Sec. III B) for the high frequency A_g and B_g symmetry modes. The highest frequency A_g^{14} and B_g^{16} modes represent TiO₆ breathing vibrations. According to the lattice dynamics calculations the bond stretching modes calculated to be between 900 and 1000 cm⁻¹ are associated with moderate or large displacements of titanium atoms. These modes can be very sensitive to the phase transition as its temperature dependence of frequency and broadening shows, Figs. 6(b) and 7. The B_g^{14} mode represents Ti—O_{1,2} stretching vibrations, Fig. 8(b). This mode is coupled with the A_g^{13} and the B_g^{15} modes below the phase transition temperature. Because Ti-atom displacements contribute substantially to the normal coordinate of these three modes, as well as to many other Raman active

modes (see Table III), we can expect an increase of the broadening (due to the orbital and spin fluctuations in Ti-ions) of almost all Raman modes of NaTiSi₂O₆ in the high-temperature phase.

In conclusion, we have measured infrared reflectivity and Raman scattering spectra of NaTiSi₂O₆ at different temperatures. The assignment of the observed modes is done using lattice dynamical calculations based on the shell model. The phase transition at about 210 K is manifested through a dramatic change of the mode frequency followed by broadening and the appearance of new phonon modes. Analyzing the phonon frequency and damping versus temperature we found that the phase transition leaves a fingerprint in the phonon dynamics of NaTiSi₂O₆.

ACKNOWLEDGMENTS

This work was supported in part by the Serbian MNTR under Project No. 1469. Z.V.P. thanks the Ministry for Education, Culture and Sport of Spain for financial support. M.J.K acknowledges support from the Research Council of the K.U. Leuven and DWTC. The authors thank W. König for low temperature far-infrared measurements.

¹M. Cameron and J. J. Papike, Am. Mineral. **66**, 1 (1981).

²M. Isobe, E. Ninomiya, A. N. Vasil'ev, and Y. Ueda, J. Phys. Soc. Jpn. **71**, 1423 (2002).

³E. Ninomiya, M. Isobe, Y. Ueda, M. Nishi, K. Ohoyama, H. Sawa, and T. Ohama, Physica B **329**, 884 (2003).

⁴M. J. Konstantinović, J. van den Brink, Z. V. Popović, V. V. Moshchalkov, M. Isobe, and Y. Ueda, J. Magn. Magn. Mater. **272–276**, e657 (2004).

⁵M. J. Konstantinović, J. van den Brink, Z. V. Popović, V. V.

Moshchalkov, M. Isobe, and Y. Ueda, Phys. Rev. B **69**, 020409(R) (2004).

⁶Z. S. Popović, Z. V. Šljivančanin, and F. R. Vukajlović, Phys. Rev. Lett. **93**, 036401 (2004).

⁷P. Millet, F. Mila, F. C. Zhang, M. Mambri, A. B. van Osten, V. A. Pashchenko, A. Sulpice, and A. Stepanov, Phys. Rev. Lett. **83**, 4176 (1999).

⁸J. L. Gavilano, S. Musholaj, H. R. Ott, P. Millet, and F. Mila, Phys. Rev. Lett. **85**, 409 (2000).

- ⁹J. Lou, T. Xiang, and Z. Su, *Phys. Rev. Lett.* **85**, 2380 (2000).
- ¹⁰M. D. Lumsden, G. E. Granroth, D. Mandrus, S. E. Nagler, J. R. Thompson, J. P. Castellán, and B. D. Gaulin, *Phys. Rev. B* **62**, R9244 (2000).
- ¹¹P. Vonlanthen, K. B. Tanaka, A. Goto, W. G. Clark, P. Millet, J. Y. Henry, J. L. Gavilano, H. R. Ott, F. Mila, C. Bertier, M. Horvatic, Y. Tokunaga, P. Kuhns, A. P. Reyes, and W. G. Moulton, *Phys. Rev. B* **65**, 214413 (2002).
- ¹²A. N. Vasiliev, T. N. Voloshok, O. L. Ignatchik, M. Isobe, and Y. Ueda, *JETP Lett.* **76**, 35 (2002).
- ¹³H. Ohashi, T. Fujita, and T. Osawa, *J. Mineral. Petrol. Econ. Geol.* **77**, 305 (1982).
- ¹⁴K. Kunc and H. Bilz, *Solid State Commun.* **19**, 1027 (1976).
- ¹⁵M. Balkanski, R. F. Wallis, and E. Haro, *Phys. Rev. B* **28**, 1928 (1983).